Journal of Structural Geology 32 (2010) 45–58

Contents lists available at ScienceDirect

Journal of Structural Geology

journal homepage: www.elsevier.com/locate/jsg

Structural geometry of Raplee Ridge monocline and thrust fault imaged using inverse Boundary Element Modeling and ALSM data

G.E. Hilley*, I. Mynatt, D.D. Pollard

Department of Geological and Environmental Sciences, Stanford University, Stanford, CA 94305-2115, USA

ARTICLE INFO

Article history:
Received 16 September 2008
Received in revised form
30 April 2009
Accepted 29 June 2009
Available online 8 July 2009

Keywords:
Monocline
Boundary element model
Airborne laser swath mapping
Inversion methods

ABSTRACT

We model the Raplee Ridge monocline in southwest Utah, where Airborne Laser Swath Mapping (ALSM) topographic data define the geometry of exposed marker layers within this fold. The spatial extent of five surfaces were mapped using the ALSM data, elevations were extracted from the topography, and points on these surfaces were used to infer the underlying fault geometry and remote strain conditions. First, we compare elevations extracted from the ALSM data to the publicly available National Elevation Dataset 10-m DEM (Digital Elevation Model; NED-10) and 30-m DEM (NED-30). While the spatial resolution of the NED datasets was too coarse to locate the surfaces accurately, the elevations extracted at points spaced ~50 m apart from each mapped surface yield similar values to the ALSM data. Next, we used a Boundary Element Model (BEM) to infer the geometry of the underlying fault and the remote strain tensor that is most consistent with the deformation recorded by strata exposed within the fold. Using a Bayesian sampling method, we assess the uncertainties within, and covariation between, the fault geometric parameters and remote strain tensor inferred using the model. We apply these methods to the Raplee Ridge monocline, and find that the resolution and precision of the ALSM data are unnecessary for inferring the fault geometry and remote strain tensor using our approach. However, the ALSM data were necessary for the mapping of the spatial distribution of surface outcrops. Our models considered two scenarios: one in which fault geometry and remote strains were inferred using a single deformed stratum, and another in which all mapped strata were used in the inversion. Modeled elevations match those observed to within a root-mean-squared error of 16–18 m, and show little bias with position along the fold. Both single- and multilayer inversions image a fault that is broadly constrained to be ~4.5–14 km in down-dip height, 13–30 km in along-strike width, with a tip-line 2.0–9.5 km below the surface at the time of deformation. Poisson's ratio was not well resolved by the inversion. The idealized elastic model is oversimplified when considering the complicated layered nature of this fold, however, it provides a good fit to the observations. Thus, comparable surface displacements may be produced with a variety of rheological models, so independent constraints on factors such as the fault geometry may be required to ascertain the appropriate rheology of the fold.

1. Introduction

The well-exposed Raplee Ridge monocline in southeastern Utah (Fig. 1) is a north-south oriented fold about 14 km long and 2 km wide (O'Sullivan, 1965; Ziony, 1966). The San Juan River has incised through the fold in the last several Ma (Wolkowinsky and Granger, 2004), exposing a thick sedimentary package (Jentgen, 1977; Ziony, 1966). Folding within the ridge likely occurred during the Laramide phase of deformation during latest Mesozoic and early Cenozoic time (Gregory and Moore, 1931). Many folds within the Colorado Plateau were formed due to reactivation of high-angle structures that likely date back as far as the Precambrian (Bump, 2003; Davis, 1978, 1999; Kelley, 1955). While no fault is exposed at the Raplee Ridge monocline and no subsurface information reveals the fault geometry, the presence of dipping beds along its west side, along with the fact that this fold is similar to many other Laramide folds in the Colorado Plateau for which faults are exposed (Tindall and Davis, 1999) or inferred (Bump, 2003; Bump et al., 1997; Davis, 1999;, Kelley, 1955) implies that this fold was formed above a east-dipping high-angle reverse fault.

As in the case of the Raplee Ridge monocline, faults that drive folding observed at the surface are often unexposed. As a result, both forward and inverse models have been used to relate fold form to the geometry of underlying faults. The simplest of these models

* Corresponding author. Tel.: +1 650 723 2782.
E-mail address: hilley@stanford.edu (G.E. Hilley).

0191-8141/$ – see front matter © 2009 Elsevier Ltd. All rights reserved.
doi:10.1016/j.jsg.2009.06.015

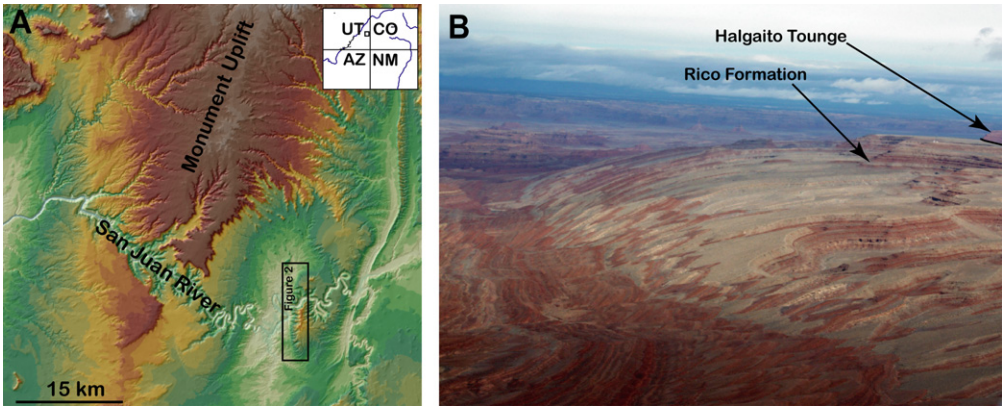

Fig. 1. (A) Shaded relief map (color-coded for elevation), showing the location of Raplee monocline in southwestern Utah. Upper right inset shows Four Corners area; location of Fig. 2 noted in location map. (B) Arial photograph of Raplee Ridge showing displacement of strata. Photo looks to the north. Fold is ~500 m in vertical relief.

are kinematic models that assume no volume change of geologic units during folding-related fault slip in order to infer the subsurface geometry of unexposed faults and the fold evolution (Allmendinger and Shaw, 2000; Bump, 2003; Cardozo, 2008; Erslev, 1991; Jamison, 1987; Mitra, 1990; Suppe, 1985). While this geometric approach may violate the stress equilibrium equations, compatibility of stresses and strains within the crust, and the constitutive stress–strain relations of the rock, it nonetheless has the appeal that computational burden is low when calculating fault and fold geometry (e.g., Allmendinger, 1998; Cardozo, 2008), and that fold forms observed in the field can be coarsely reproduced. However, with the advent of high-speed computers, we now have the ability to create forward models that satisfy the constitutive stress–strain relations, stress–strain compatibility, and the equations of static equilibrium in the crust (e.g., Casey and Butler, 2004; Guiton et al., 2003). Such forward models have been developed for materials that are linear elastic (Bellahsen et al., 2006; Fiore et al., 2007; Shamir and Eyal, 1995), linear viscous (Johnson and Johnson, 2001, 2002), nonlinear elastoplastic with frictional faults (Sanz et al., 2007), and nonlinear viscous with frictional faults and bedding surfaces (Sanz et al., 2008). Each of these models assumes that the crust is in a state of static stress equilibrium, and so the component of the momentum budget that arises from accelerations (e.g., individual earthquake rupture dynamics) is small. Some of these models have been used to infer the kinematics of slip on prescribed faults (Bürgmann et al., 2005; Maerten et al., 2005), or loading and fault geometry in two dimensions (Johnson and Johnson, 2002). Thus, the ability to use a fully mechanical approach that infers fault geometry and loading conditions from surface observations now exists (Mynatt et al., 2007).

The National Center for Airborne Laser Mapping (NCALM) collected ALSM topographic data funded by the National Science Foundation Collaborations in Mathematics and Geosciences (NSF-CMG) program that images the deformed strata at Raplee Ridge (Fig. 2a). These data provide a high precision, dense array of points on patches of marker bedding surfaces that we use to infer the subsurface geometry of the fault that may be responsible for the monocline. Our previous work at Raplee Ridge (Mynatt et al., 2007) combined the ALSM data with an elastic boundary element model to infer the geometry of the fault. The present study builds on this previous work by jointly estimating Poisson's ratio of the modeled fold, and implementing a scheme that uses multiple layers and observations of bedding-plane rotations to constrain the fold geometry.

In this contribution, we compare the ALSM data to other more commonly available topographic data (Fig. 2b and c) to determine what spatial resolution is required to infer the subsurface geometry of faults based on the displacements of exposed folded strata. In addition, we expand the previously described method to use a series of layers within the fold in order to better constrain the geometry of the underlying structure. We use a Markov–Chain Monte Carlo method to provide an estimate of the variation within, and covariation between, model estimates of fault geometry parameters that produce deformation similar to that recorded within the fold.

2. Study area

Raplee Ridge monocline (Fig. 1) is located in southeast Utah, east of the town of Mexican Hat Mynatt et al., 2009. This structure lies west of the laterally continuous Comb Ridge monocline, which strikes N-S to NNE-SSW in this area (Kelley, 1955; Fig. 1, Ziony, 1966). The orientation of folded strata exposed within the Comb Ridge monocline is consistent with slip along an underlying W- to WNW-dipping fault that strikes parallel to the trend of the monocline. Unlike this more extensive structure, which can be traced for 10s of kilometers along its strike, Raplee Ridge is spatially restricted to ~15 km along its N-S strike. No subsurface data in this area image the relationship between the Raplee Ridge monocline and structures that accommodate the displacement along the Comb Ridge monocline in the subsurface; however, it is plausible that a fault that drives folding seen in Raplee Ridge serves as a backthrust to the larger Comb Ridge fault. If this were the case, the thrust fault geometry may shoal as the deeper basement backthrust advances into the mechanically weak strata above, as has been seen in other reactivated basement-involved structures (e.g., Narr and Suppe, 1994).

The strata exposed within Raplee Ridge include the Pennsylvanian Paradox Formation to Permian Halgaito Tongue, but here we focus on the Rico Formation, which consists of alternating limestones, siltstones, and sandstones that record a general trend of marine regression up-section. The occurrence of marine incursions during this generally regressional sequence has resulted in the deposition of five limey sandstone and sandy limestone layers encased within shales and siltstones that currently provide well-exposed stratigraphic markers whose surfaces reveal the geometry of the fold (Fig. 3). These marker layers are folded into the ~500 m high doubly plunging monocline. Sedimentary layers within the monocline's forelimb dip up to 40° to the west, in contrast to those gently dipping (<5°) to the east within the backlimb (Figs. 1 and 2).

Exposure of different stratigraphic markers varies depending on the depth of incision into the fold. The surface of the highest stratigraphic level used as part of this study, the McKim limestone, is widely exposed throughout the fold due to the fact that erosion

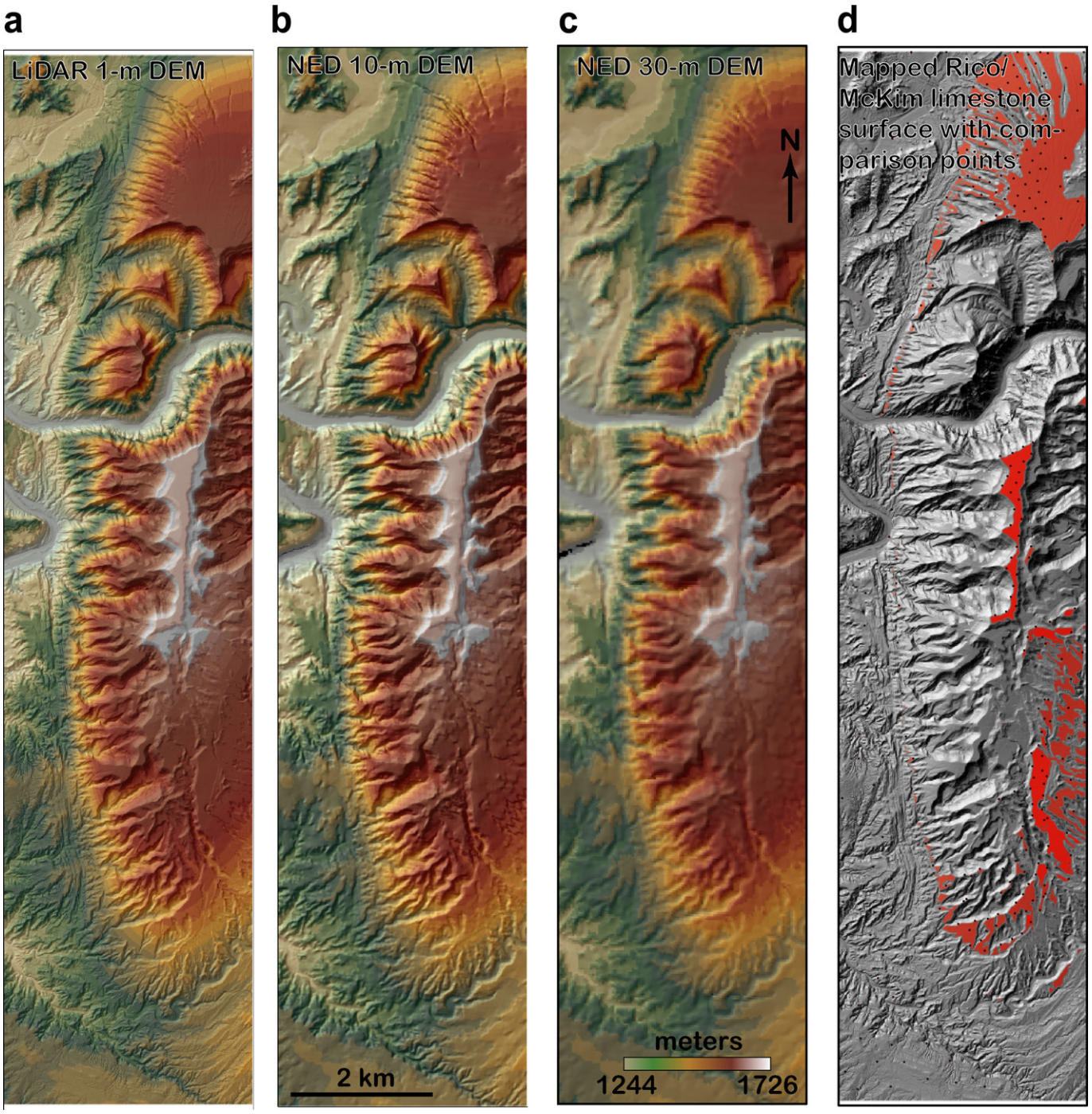

Fig. 2. The topography of Raplee Ridge, as imaged by the (a) 1-m ALSM-derived data, (b) NED-10 data, and (c), NED-30 data. All elevation maps have the same elevation and map-view scale. (d) Shaded relief map showing the mapped extent of the McKim surface used in single-layer inversions. The location of (*x*,*y*,*z*) points extracted and used to compare accuracy of different datasets are shown as red dots. Note that the mapped surface constrains the shape of the fold at a particular stratigraphic depth.

has stripped virtually all of the overlying Halgaito Tongue from this surface over much of the fold (Fig. 3). Within basins incised into the fold, four additional marker layers define the fold's geometry including, from top to bottom, the Goodrich, Shafer, Mendenhall, and Unnamed limestones (Mynatt et al., 2009). Within these basins, individual bedding surfaces can be identified and mapped; however, the exposure of these four lower units is often restricted to limited areas of the fold hinge that have been excavated by erosion. Overlying the McKim limestone, exposure of the Halgaito Tounge shale along the peripheral edges and away from the fold constrains the extent of the fold by defining those areas that are less deformed.

Throughout the Colorado Plateau, similar monoclines are often associated with Laramide contraction that occurred during late Mesozoic through early Cenozoic time (Davis, 1979; Kelley, 1955; Reches, 1978; Reches and Johnson, 1978). Where exposed, at least some of these structures appear to result from movement along high-angle basement faults that may have first experienced motion as early as the Proterozoic (e.g., Davis, 1999, and references therein; Huntoon, 1993; Huntoon and Sears, 1975; Kelley, 1955). In some

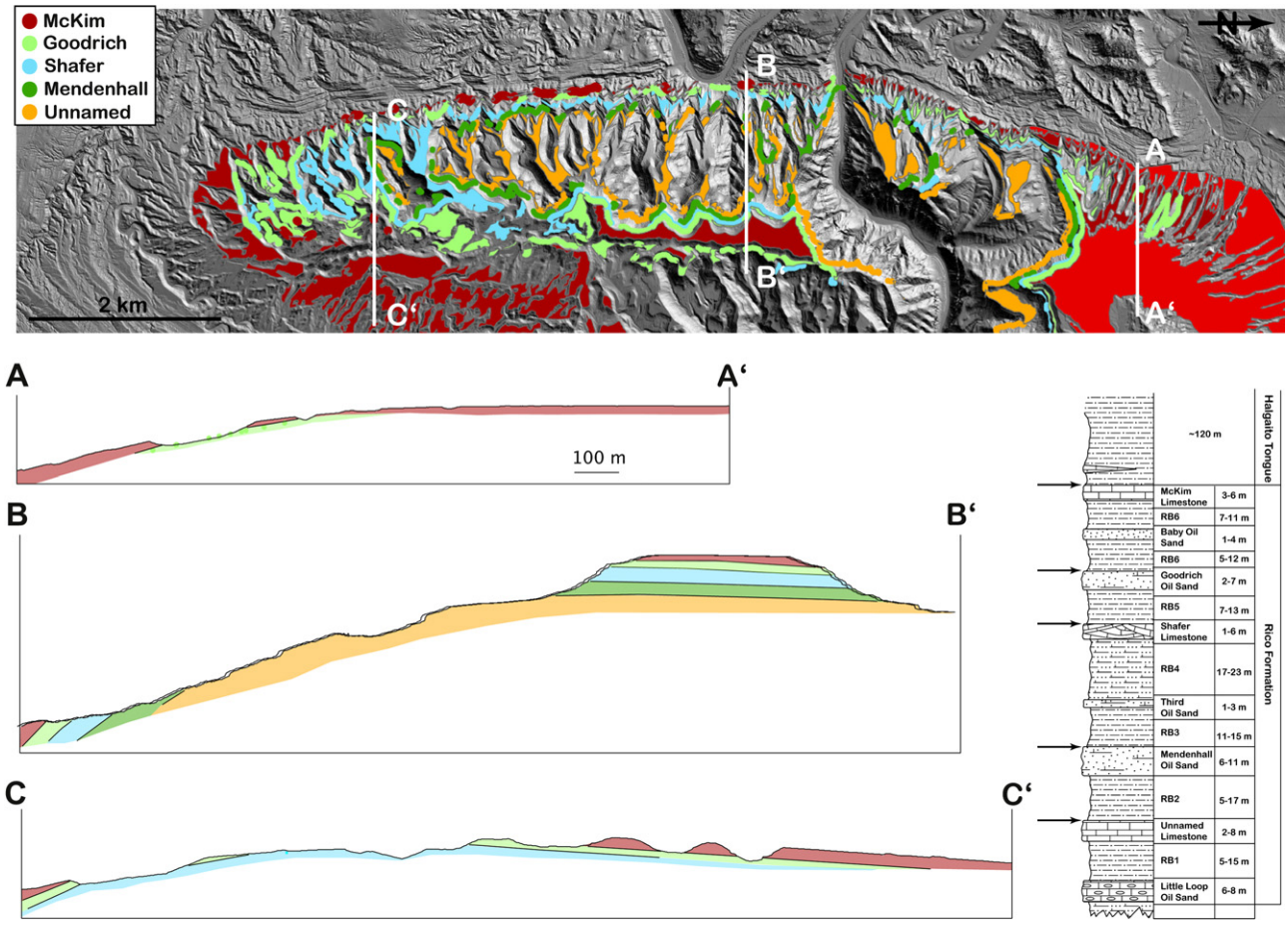

Fig. 3. Shaded relief map showing the spatial distribution of the five bedding-plane surfaces exhumed within the fold. From stratigraphically highest to lowest, they are the McKim, Goodrich, Shafer, Mendenhall, and Unnamed surfaces. Location of structural sections are noted in geologic map. Structural sections have no vertical exaggeration. Arrows in the stratigraphic column note the stratigraphic position of the top of each of the bedding surfaces shown in the geologic map.

cases, the reverse faulting that deformed Colorado Plateau strata into monoclinal geometries were subsequently reactivated during Basin and Range extension in the Miocene (e.g., Huntoon and Sears, 1975). However, where this can be shown to be the case, normal-sense reactivation of the basement faults caused them to propagate through the strata above. Thus, Laramide contractional deformation is often accommodated within the Paleozoic and Mesozoic section by warping of the strata, whereas later extensional deformation typically resulted in discrete offset of these units (Huntoon and Sears, 1975). At Raplee Ridge, detailed field observations show that there are no faults that link with the underlying basement structures; thus, we infer that the deflected strata within the monocline result from Laramide contraction, rather than Miocene extension. Consequently, the western monoclinal forelimb implies that an underlying reverse fault likely dips towards the east. By analogy with other basement-involved structures, it is possible that the geometry of the fault steepens as it enters the basement rocks upon which the folded strata were deposited (e.g., Narr and Suppe, 1994).

3. Airborne Laser Swath Mapping (ALSM) data

On February 24, 2005, the National Center for Airborne Laser Mapping (NCALM) collected topographic data from the Raplee Ridge area using an Optech 25 kHz pulsed laser range finding system and associated Inertial Measurement Unit (IMU) that is corrected for drift using kinematic GPS observations taken onboard the aircraft. The acquisition was performed to build a fold-scale geometric model to compare outcrop-scale measurements of fracture characteristics to fold geometry (Mynatt et al., 2009). The combination of acquisition frequency and low elevation flight plan provided several laser range positions per square meter from which a 1-m Digital Elevation Model (DEM) was produced by kriging interpolation (Isaaks, 1989). The vegetation at the site proved sufficiently sparse to obviate the need for spatial filtering to remove its contribution from the DEM (Fig. 2). From this 1-m DEM, a shaded relief map of the fold was produced, which was used in the field to map the extent of the uppermost surface of the five stratigraphic markers throughout the fold (Figs. 2d and 3).

The markers range in thickness as follows (Ziony, 1966): Unnamed, 2–8 m; Mendenhall, 6–11 m; Shafer, 1–6 m; Goodrich, 2–7 m; and McKim, 3–6 m. Accurate mapping of the top surfaces of these thin layers required the 1-m DEM. Once the marker surfaces were identified and mapped on the georeferenced images, (x,y,z) points that defined the geometry of each of the surfaces were extracted from the DEM. In some cases, the topographic surfaces that appear to define the tops of the mapped strata have been modified by up to 1 m by surface processes. In addition, erosion along the up-slope edges of the surfaces has distributed a small amount of colluvium (typically less than 1 m thick) onto the tops of the exposed strata. Thus, we estimate the precision of elevation estimates to be $\sim$ 2–5 m (Mynatt et al., 2007).

More than 100,000 points were extracted from the mapped stratigraphic surfaces. Consideration of this large number of points would render intractable the fold-scale inversion described below.

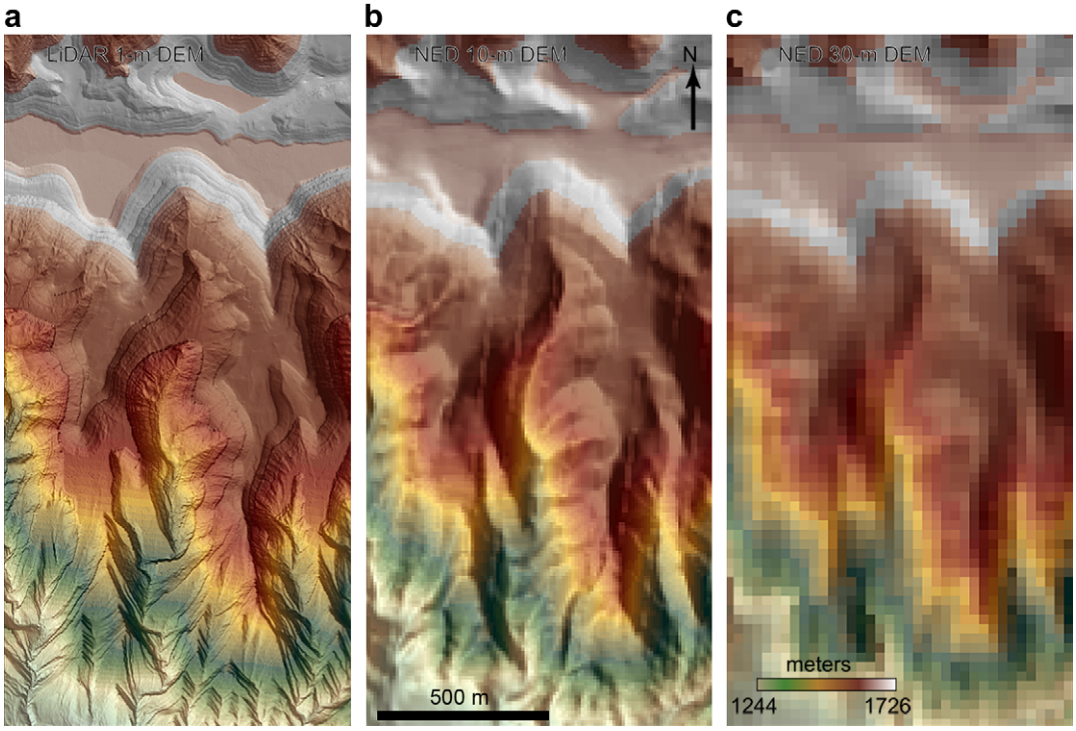

Fig. 4. Color-coded, shaded relief DEM of the center of Raplee Ridge, showing the detailed differences in resolution between the datasets. (a) The ALSM-derived DEM, (b) the NED-10 DEM, and (c) the NED-30 DEM. Color and map-view scales for all panels are identical.

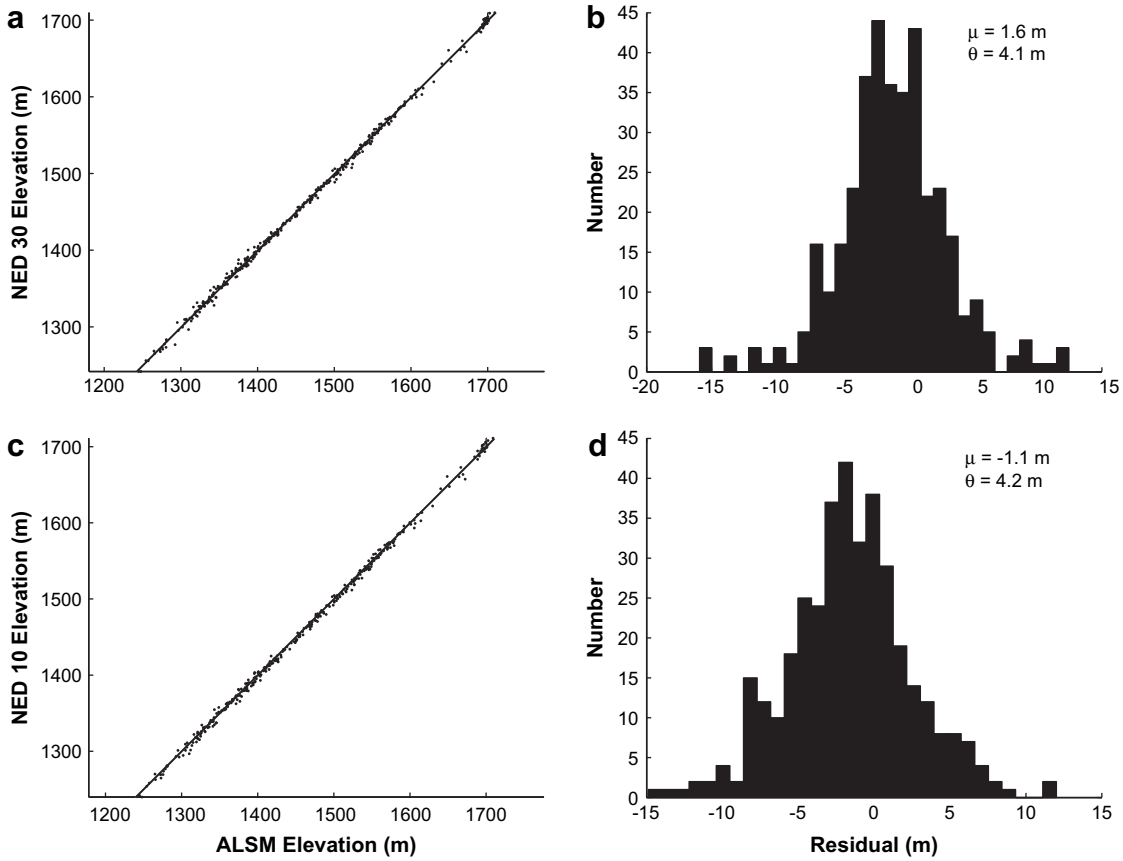

Fig. 5. Comparison of elevations derived from ALSM data with those derived from (a) the NED-30 DEM, and (c) the NED-10 DEM. The residual, or difference between the NED-30 (b) or NED-10 (d) and ALSM data, are shown as histograms, with the mean and standard deviations of these distributions noted in each panel.

For this reason, we decimated the dataset to provide (x,y,z) points for each of the surfaces that were spaced no less than 50 m apart. We compared the ALSM measurements of these extracted points to more commonly available datasets to assess the precision of data for use in this study.

Specifically, we compared equivalent z values at the selected (x,y) points to those extracted from the National Elevation Dataset (NED) 30-m resolution DEM and 10-m resolution DEM. The poor spatial resolution of both NED datasets relative to the ALSM data would prohibit accurate identification and mapping of the extent of the different stratigraphic marker surfaces within the fold (Fig. 4), although low elevation air photos that were precisely georeferenced might be employed for such a purpose. However, despite the coarse resolution of both NED datasets, their extracted elevation values compared favorably with those obtained from the decimated ALSM dataset (Fig. 5a,c). To provide a quantitative metric of the differences between these three datasets, we calculated the residual elevation by subtracting the elevation value at each (x,y) point used in this study for both NED datasets from the elevation at corresponding (x,y) locations in the ALSM dataset (Fig. 5b,d). Elevations from both NED datasets showed little, if any bias in elevation relative to the ALSM data. The mean residual value equaled 1.6 m and −1.1 m for the NED 30-m and 10-m datasets, respectively, relative to the ALSM dataset. Variation between these two datasets was modest: standard deviation in residuals from NED 30-m and 10-m datasets was 4.1 and 4.2 m, respectively. However, as described below, the average misfit for our best-fit inversions was several times this variation. Thus, given the uncertainties in the fold-wide inferences produced by modeling, elevations extracted using the NED 30-m and NED 10-m datasets should supply adequate precision when using these data as inputs to the fault geometry inversions described below. This conclusion presupposes that geologic mapping can provide accurate locations of the stratigraphic marker surfaces.

4. Methods

4.1. Inversion methods

The two major goals of this study were to provide a detailed and accurate depiction of the continuous structural geometry of Raplee Ridge monocline that could be compared to outcrop-scale measurements of fracture characteristics (Mynatt et al., 2009), and to infer the geometry of and remote strain conditions acting along the reverse fault underlying the monocline. The finite extent of the Raplee Ridge monocline necessitated the use of a three-dimensional model that could capture the along-strike variations in fault and fold geometry (e.g., Figs. 1 and 2). Some three-dimensional models that conserve the area and length of strata exist (Gratier et al., 1991); however, as outlined above, such methods do not take advantage of the constraints provided by a full mechanical analysis. Likewise, methods that use a complete mechanical analysis to relate displacements to the geometry of underlying strata assume two-dimensional plane-strain conditions (e.g., Cooke and Pollard, 1997; Johnson and Johnson, 2002; Sanz et al., 2007; Sanz et al., 2008), and thus cannot adequately capture the three-dimensional nature of the Raplee Ridge monocline. Some recent studies point the way towards estimating fault geometry and loading using forward three-dimensional elastic models (e.g., Bellahsen et al., 2006; Fiore et al., 2007). We build on these types of studies by using formal nonlinear inversion methods to estimate fault geometry and loading conditions as initiated by Mynatt et al. (2007).

In this study, we used the three-dimensional Boundary Element Model (BEM) Poly3D to relate the displacement of strata to underlying fault geometry and loading conditions (Maerten and Maerten, 2008; Maerten et al., 2006; Tamagawa and Pollard, 2008; Thomas, 1993). This BEM idealizes the rheology of Earth's brittle upper crust as homogeneous, isotropic, and linear elastic. Triangular planar elements are embedded into this elastic material to represent parts of faults and fractures along which displacement within the material is discontinuous. Slip or opening along these elements is driven either by specifying the displacement discontinuity directly, allowing the elements to slip under a prescribed remote loading (assuming zero friction acting along the fault surface elements), specifying a stress drop along the elements, or any combination of these boundary conditions for the normal and two shear components. For example, one may specify mixed-mode boundary conditions in which shear tractions acting across an element induce slip parallel to the element, while prescribing a zero displacement condition perpendicular to the element (no opening/closing). A set of triangular elements may be assembled to produce an arbitrarily complex surface in three dimensions along which any combination of displacement discontinuity or stress drop boundary conditions may be specified. Finally, the BEM can calculate fault slip distributions along the fault(s), stresses/strains within the surrounding medium, and displacements within a half or full-space problem. The half-space model is used to compute stresses, strains, and displacements given the presence of a traction-free surface that represents the interface between the solid earth and atmosphere, while the full-space model may be used to approximate faulting processes deep within the crust.

In this study, we assume that displacements of stratigraphic marker layers are produced by slip along a single, elliptically shaped, frictionless planar fault underlying the monocline. Its elliptical geometry approximates the three-dimensional extent of many faults documented in the field (e.g., Willemse et al., 1996), while

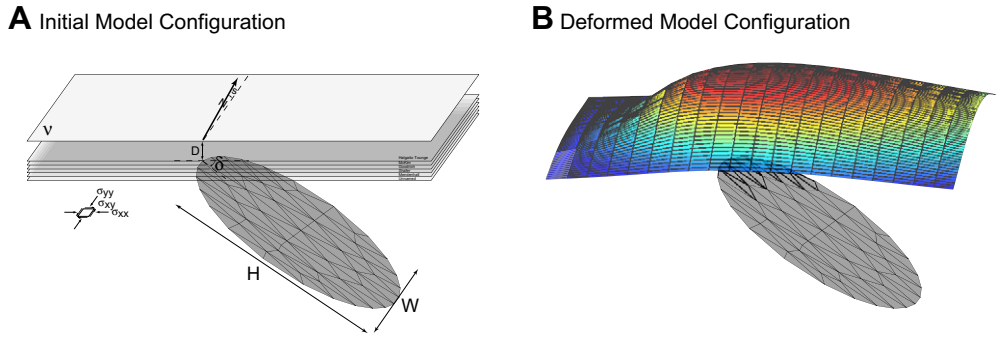

Fig. 6. Schematic model setup, showing the definition of each of the parameters used to define the fault geometry and loading conditions in the Poly3D model. Model parameters shown in the figure are defined in text. (A) Model parameters, (B) deformed model configuration.

ignoring geometric complexity that would be difficult to constrain using displacements inferred from the ALSM data. Likewise, we chose a planar fault geometry to mimic the geometry of older reactivated basement faults (Davis, 1978; Huntoon and Sears, 1975; Tindall and Davis, 1999). We acknowledge that the geometry of the fault underlying this monocline is likely more complex than this simple geometry; however, as we show below, even this simple idealization of the underlying fault geometry produces displacements that closely mimic those observed at Raplee Ridge monocline. Others have proposed non-planar geometries for such faults (e.g., Narr and Suppe, 1994); however, given the lack of additional information to constrain the at-depth geometry of this fault, we have chosen the simplest possible geometry that is harmonious with available observations. Should additional data become available that better constrain the at-depth geometry of the Raplee Ridge fault, it is straightforward to assimilate this information into our modeling approach.

Given this idealization, the geometry and location of the fault underlying the fold is defined by 9 parameters (Fig. 6): the down-dip length of the fault (H), the along-strike width of the fault (W), the depth of the fault below the surface (D), the map-view location of the fault relative to the coordinate system of the model (x_o,y_o), the dip of the fault (δ), the strike of the fault (s), and the remote conditions that drive motion along the fault. In this study, slip along the fault results from a prescribed remote strain tensor (ε_{xx}, ε_{yy}, ε_{xy}), which we assume does not vary with depth. We also set $\varepsilon_{zz} = \varepsilon_{xz} = \varepsilon_{yz} = 0$. We use this remote strain to compute the stresses acting along the fault elements, and compute shear displacements that result from this load. Dimensional analysis shows that Young's modulus is not an independent free parameter in our model, since we prescribe remote strain boundary conditions and calculate only surface displacements. If we were to use the stress state in the crust during deformation as an additional constraint, Young's modulus would again enter the analysis. We prohibit opening or closing perpendicular to the fault surface, as large amounts of opening or fault-zone contraction are physically unrealistic at depths of >1.5 km that likely typify the shallowest levels of slip along this fault during late Mesozoic time (see below).

Once the fault geometry and loading conditions are specified, the BEM calculates stresses, strains, and displacements at specified points in the surrounding rock mass. These displacements can be used to calculate the displacement of initially flat surfaces, such as the stratigraphic marker layers currently exposed at Raplee Ridge. We reconstructed the relative elevation and stratigraphic thickness of each of the five surfaces modeled in this study using the measured stratigraphy (Mynatt et al., 2007; Ziony, 1966) as well as ALSM-based thickness measurements from flat-lying portions of the stratigraphy exposed by downcutting of the San Juan River (Mynatt et al., 2009). The likely depth of each of these units was then inferred by noting that during late Mesozoic time, approximately 1.2 km of sedimentary rocks locally overlaid the section under study (Hodgson, 1961). Thus, we were able to use this information to estimate the depth of the originally flat-lying strata at the time they were deformed.

As these units deformed, points originally located on the flat-lying surfaces were displaced both vertically and horizontally. Thus, the current location of the observed points along deflected layers do not record their initial positions faithfully, especially in the case that surface displacements are large. The BEM calculates the displacement of a given point that is defined prior to deformation; however, the displaced points measured using the ALSM dataset record each point's final, rather than initial position. We calculate the appropriate displacement at each (x,y) observation point on the deformed-state surfaces using a two-step process. First, we calculate a regular grid of displacements for each stratigraphic level that results from a specified set of fault geometric and remote loading parameters. These regularly spaced points are deformed into an irregularly shaped mesh that represents the final configuration of each deformed surface. This process results in a set of irregularly spaced points on the deformed surface for which we know displacements that are required to restore the points to a regular grid. Using the deformed configuration, we use a linear interpolation to map these displacement values to the (x,y) locations of each of the ALSM measurements, and use these interpolated displacements to restore each point to its initial location on the undeformed surface. In a second step, we use identical input parameters with the BEM to deform these initial state points into the final state to determine the geometry of the deflected surface. This results in (x,y) coordinates of the new deformed state points that match the locations of the observations, and allows us to directly compare the elevation values observed to those that are predicted by the BEM.

The above approach is appropriate for comparing observations of the elevation of each deflected surface to those predicted by the BEM. However, in some instances, such as our observations along the Halgaito Tounge surface, the rotation of bedding rather than its absolute elevation helps to constrain the fault geometry. In this case, we employ a similar approach to that used for elevation values; however, instead of calculating displacements at each of the points, we instead calculate bedding-plane rotation. As before, we first restore the observation locations on each of the surfaces for which bedding rotations are measured to their original locations. However, we use the initial-state locations to calculate rotation of these points as they are deformed and compare these rotations to observations. This was used to enforce areas of no rotation (e.g., flat-lying sediments as seen to the west of the fold).

Using these methods, we calculate the elevation values that would be predicted by a given set of fault geometry and loading parameters, and compare them to the observed elevation values for each layer using the following misfit function:

$$\mathrm{WRSS} = W_z \sum_{i=1}^{n} \left(\left[\frac{z_i^{\mathrm{obs}} - z_i^{\mathrm{pred}}}{\sigma_i^{\mathrm{zobs}}} \right]^2 \right) + W_r \sum_{j=1}^{m} \left(\left[\frac{r_j^{\mathrm{obs}} - r_j^{\mathrm{pred}}}{\sigma_j^{\mathrm{robs}}} \right]^2 \right) \quad (1)$$

where z^{obs} are the ALSM-derived elevations of the deflected strata at the (x,y) locations, σ^{zobs} are the standard deviations of the elevation measurements, z^{pred} are the predicted elevations from the BEM, W_z is the weight given to the misfit between measured and observed elevation values, r^{obs} are the observed rotations (only flat-lying portions of the Halgaito Tounge member are used in areas away from the fold to constrain its extent), σ^{robs} are the standard deviations of the rotation measurements, r^{pred} are the predicted rotations from the BEM, W_r is the weight given to the misfit between measured and observed rotations, and WRSS is the weighted residual sum of squares misfit function. As WRSS values decrease, the displacements and rotations calculated by the BEM better match those observed. Thus, we can find the best-fitting fault geometric and loading parameters (hereafter referred to cumulatively as "model parameters") by exploring various values of these model parameters, calculating the misfit defined by Eq. (1), and identifying the model parameters associated with the minimum value of the WRSS.

In addition to the best-fitting model parameters, we quantify the uncertainty in these model estimates using a Bayesian sampling method. In this approach, the model parameters are viewed as a joint probability density function (pdf), the number of whose dimensions corresponds to the number of model parameters. Such a joint pdf may be used to determine both the best-fitting set of model parameters and uncertainties within and covariation between model parameters. These measures can be used to quantify the uniqueness of the best-fitting solution, and to provide information

about those combinations of model parameters that provide similar fits to the observed data. We calculate this joint pdf of the model parameters using Bayes' Rule (Bayes, 1763):

$$P(m|x) = \frac{P(x|m)P(m)}{\sum_{j=1}^{n} P(x|m_j)P(m_j)} \quad (2)$$

where x is a vector consisting of the observations, m is a vector consisting of the model parameters, $P(m|x)$ is the joint pdf of the model parameters given the observations, $P(x|m)$ is the probability of the data given the model parameters that can be derived from a misfit function similar to Eq. (1), $P(m)$ is a pdf that represents the probability of occurrence of the model parameters in the absence of any observations, and the denominator normalizes the cumulative density of $P(m|x)$ to unity (e.g., Bayes, 1763; Hilley and Young, 2008a,b). $P(m|x)$ is often referred to as the posterior density while $P(m)$ is referred to as the prior density.

Bayes' Rule is used to estimate $P(m|x)$ in our analysis as follows. First, a set of model parameters (m) is selected and from these choices, predicted elevations and rotations are computed at all points for which we have measured values of these quantities. The probability of observing the data given the model parameters, $P(x|m)$ is computed using a modified version of Eq. (1) that takes into account the number of degrees of freedom (DOF; defined as the number of observations minus the number of model parameters) in the model and the uncertainty associated with each elevation or rotation observation (e.g., Pollitz, 2003, and references therein):

$$P(x|m) = \exp\left(-\chi_r^2\right) \quad (3a)$$

where

$$\chi_r^2 = \frac{\mathrm{WRSS}}{\mathrm{DOF}} \quad (3b)$$

Bayes' Rule also requires the definition of the prior density $P(m)$. This prior density represents the probability that a set of model parameters occurs in the absence of any data to which the model is compared. This prior density may represent some quantitative a priori information about various aspects of the fault geometry or loading conditions, or simply may be used to incorporate expert opinion into the statistical analysis. For example, at a particular site, subsurface seismic data may resolve a range of permissible fault geometric parameters, such as fault strike and dip. This prior information constrains the geometry of the fault in the absence of any mechanical modeling or measurements of bedding displacement. We cast these ranges in the fault geometric parameters in terms of the probability of each value's occurrence as a pdf. By repeating this process for all of the model parameter values, we construct the prior pdf $P(m)$ that represents our prior knowledge of reasonable ranges in fault geometry. In the case of the Raplee Ridge monocline, we do not have additional prior information that constrains the geometry of the underlying fault, and so we simply specify a uniform probability of $P(m)$ for all values of the model parameters, m. Thus, Eq. (2) reduces to

$$P(m|x) = \frac{P(x|m)}{\sum_{j=1}^{n} P(x|m_j)} \quad (4)$$

By evaluating $P(x|m)$ for all permissible values of m, we can use Eq. (4) to compute the probability of occurrence of the model parameters, $P(m|x)$.

The simple mechanical model used to compute $P(m|x)$ requires nine parameters to be specified, and hence, m consists of a nine-dimensional parameter space. If each dimension of the parameter space were discretized into only ten values, the number of evaluations of the BEM that would be required to compute $P(m|x)$ would be 10^9, or one billion different combinations of model parameters. Such a large number of evaluations is computationally infeasible given current computing technology. Indeed, it is this limitation that has prevented the direct application of Bayes' Rule to all but the simplest problems with few model parameters. To circumvent this difficulty, Markov–Chain Monte Carlo (MCMC) methods have been developed that sample the underlying distribution $P(m|x)$ in a computationally efficient way to provide a numerical approximation of this distribution. In these methods, sparse sampling of $P(m|x)$ is performed by the MCMC sampler, which is designed to sample $P(m|x)$ according to the pdf's underlying probabilities. In this way, the portions with high $P(m|x)$ can be identified using only a small fraction of the evaluations that would be required to exhaustively explore the entire parameter space.

The sampler employed in this study is the Metropolis–Hastings MCMC method (Metropolis et al., 1953). In this algorithm, The Metropolis–Hastings sampler uses a selection–rejection criterion to guide sampling through the parameter space such that $P(m|x)$ is approximated. We first use an initial, randomly selected choice for m—the exact choice for this starting point becomes less important as the simulation proceeds and the sampler instead selects points based on the underlying distribution $P(m|x)$. After this choice has been made, a set of random numbers is drawn from the interval $[-1,1]$, one for each dimension of m. These numbers are then scaled by a specified, arbitrary constant and added to the previous choices for the initial model parameters, moving the samples a random distance through the parameter space, m. This is the selection process. Next, this new set of samples may be either accepted or rejected. If accepted, the new samples are treated as a new starting point for the sampler and the selection process is repeated. If the samples are rejected, the previous values of the model parameters are used to select a new set of samples. Samples are accepted or rejected based on the probability of their occurrence relative to the probability of occurrence of the previous set of samples. First, the probability of occurrence for both the previous set of samples and the current selection of samples is computed using Bayes' Rule (Eq. (4)). We define the probability of the first sample as P_1, whereas the probability of the second sample is denoted as P_2. In the case that $P_2 > P_1$, the new set of samples is always accepted. However, if $P_2 < P_1$, the ratio of these two probabilities is computed and compared to a random number drawn along the interval [0,1]. If the ratio exceeds this random number the sample set is accepted, otherwise it is rejected. Thus, the Metropolis–Hasting sampler explores the parameter space m, is guided towards higher values of $P(m|x)$ in Eq. (4), and the frequency of the model parameters chosen by the sampler approximates the posterior density $P(m|x)$. Initially, the values selected by the sampler will depend on the arbitrary initial choices for the model parameters at the beginning of sampling; however, as sampling proceeds, the memory of these initial choices tends to fade and the frequency of m selected by the sampler will reflect $P(m|x)$. Thus, a "burn-in" period of sampling is used to erase the memory of the arbitrary sampling starting location in the parameter space, and only samples drawn after this burn-in are used when computing $P(m|x)$. In our study, we allow a burn-in period of 50,000 samples to allow sample choices to become independent of the initial choices for the model parameters, and collect 100,000 samples to approximate the posterior pdf, $P(m|x)$.

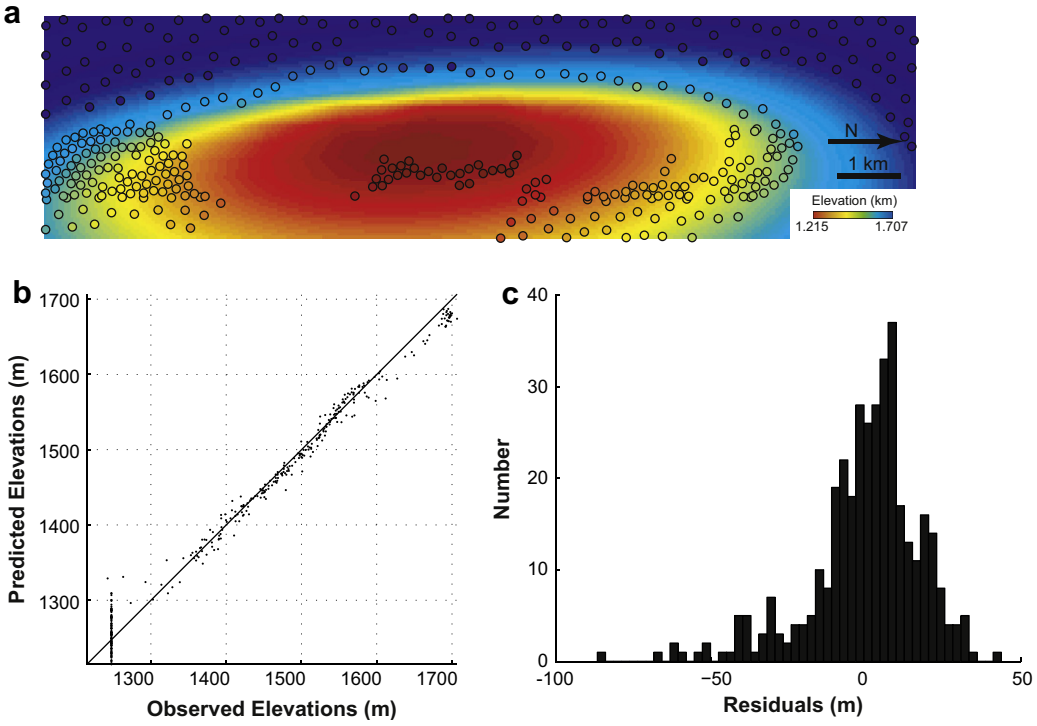

Fig. 7. (a) Observed (filled circles) and predicted (shaded background) elevations of the McKim surface that are produced as an initially flat layer is deflected by movement along the best-fitting modeled fault geometry that slips in response to the best-fitting remote strain conditions. (b) Plot of observed versus predicted elevations and (c) histogram of residual elevations (observed elevations minus best-fitting modeled elevations) that are produced by the best-fitting modeled fault geometry and loading conditions.

4.2. Modeling Raplee Ridge monocline

We used the BEM to calculate bedding-plane displacements due to slip along a blind reverse fault for two scenarios–one in which only the most well-exposed bedding surface (McKim surface) was used to compare observed and modeled fold geometry, and a second in which all mapped bedding surfaces were used to define the fold's geometry (Fig. 6). The first of these two scenarios is similar to the inversion presented in Mynatt et al. (2007), except that in this study, the misfit is normalized by the number of degrees of freedom in the model. This difference does not impact the values of the model parameters that best match the observed elevations; however, the uncertainties associated with each model parameter tend to be larger (and likely more realistic) than those presented in Mynatt et al. (2007).

Elevation estimates along the mapped surfaces are available every square meter using the ALSM data. For expediency, we consider only a subset of points separated by a minimum distance of 50 m when inverting for the fold's geometry. This reduces the number of computations necessary by a factor of ~2000. The Metropolis–Hastings inversions described above require several weeks to ~1.5 months of computation time on a dual 1.6 GHz Mac OS XServe server using this low-resolution dataset, and so inversions that use the full-resolution data would be infeasible given today's computing technology.

The mapped surfaces are not exposed within the forelimb syncline of the fold. Thus, the observations of the mapped bedding surfaces permit a fold geometry in which layers continue to dip westward at great distances west of the extent of exposure of these surfaces (Fig. 2b). However, surfaces exposed along unmapped higher bedding surfaces within the stratigraphic section show subhorizontal orientations, indicating that the mapped units share a similar orientation in the subsurface. To account for these observations, we used two different approaches. In the case of the models that considered only the observed geometry of the McKim surface, we assumed that the stratigraphic thickness between the exposed units and the McKim bedding-plane surface within the fold's eastern portion was similar to that observed in locations far from the fold-related deformation. This thickness was used to infer the depth at which the McKim surface should be located in the subsurface. These inferred (x,y,z) subsurface locations were used when inverting for the fold's geometry. In the case where we considered all mapped layers in the inversion, we instead used a rotation constraint within the Halgaito Tongue member, which is well exposed throughout the area surrounding the fold. In this way, rather than assign subsurface locations for which the (x,y,z) locations of each of the bedding planes is located, we instead required areas at the stratigraphic level of the Halgaito Tongue member to experience no rotation (right-hand term in Eq. (1)). This has a similar effect of ensuring that the geometry of the fold is finite in areas to its west.

5. Results

We first present the results of our fold inversion when only comparing elevation values measured along the McKim surface to elevations of the deflected surface that were predicted by the BEM. The best-fit model (Fig. 7) shows that the observed fold geometry is most consistent with a fault whose width is almost three times its down-dip length (best-fitting model parameter values shown as italic numbers in each model parameter panel of Fig. 8). In addition, the forelimb dips indicate that the tip-line of the fault is likely only several hundred meters below the current surface in the fold's center. The strike of the underlying fault is approximately 3° east of north, consistent with the roughly N-S trend of the observed topography. In addition, the fault underneath the fold is inferred to dip ~47° to the east. Poisson's ratio of the sediments overlying the fold inferred by the model (0.28) is close to that typically assumed for crustal rocks (Jaeger and Cook, 1969). Finally, the regional contraction in the E-W direction

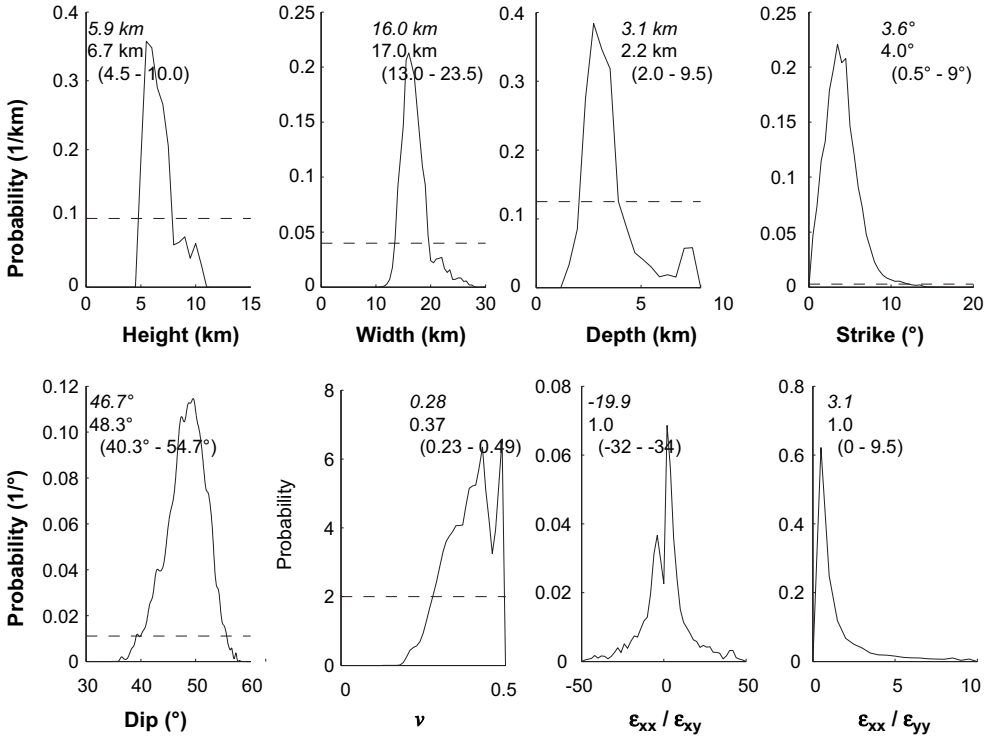

Fig. 8. Posterior probability density functions of each of the model parameters for single-layer (McKim surface only) model inversions. In each panel, the solid line denotes the probability density of each model parameter given the elevations observed along the McKim surface, while the dashed lines show the prior probability (assumed uniform in this study) assumed for the model parameters. Numbers in italics represent the value of each parameter for the best-fitting model, while solid bold numbers represent the mean value produced by all simulations. The range shown in parentheses represents the 95% bounds on the model parameter values determined from the posterior probability density function.

(ε_{xx}) is expected to be ~3 times that in the N-S direction (ε_{yy}), and is ~20 times larger than the regional shear strain (ε_{xy}). The absolute value of E-W strain (ε_{xx}) for the best-fitting model was 0.43.

The best-fitting model produced surface elevations consistent with those measured (Fig. 7a). The quality of the fit is seen on a graph of observed versus predicted values (Fig. 7b) at points where elevations were extracted from the ALSM data (locations of points shown in Fig. 7a). The inferred subsurface points along the western portion of the fold were assigned a constant value, which appear as a vertical line of points at low elevations in Fig. 7b. In contrast, calculated displacements vary smoothly across these points, creating a mismatch between the inferred subsurface elevations and those predicted by the BEM. The residuals (defined as the modeled elevations minus the observed elevations) show approximately zero mean. In addition, the model systematically underestimated points at the crest of the fold, which skewed residuals negatively (Fig. 7c).

The best-fitting model yielded a root-mean-squared error of 16.1 m. This value is significantly greater than the uncertainty in the elevation observations, indicating the mismatch between elevations predicted by the linear elastic half-space model and those observed is far larger than the uncertainties in elevation that we measured using the ALSM. Indeed, given the high accuracy of the ALSM elevations (< 2–4 m), it is difficult to conceive of an idealized model (of any rheology) whose average misfit might be on the order of, or less than this value. Thus, the high accuracy of our data relative to that expected from our idealized model forces us to conceptualize σ^{obs} in Eq. (1) as the inaccuracy that is produced by the strict model assumptions of the BEM. In this context, we adjust σ^{obs} in Eq. (1) to require that $\chi^2_r = 1$ for the best-fitting set of model parameters. As we see below, this choice for σ^{obs} increases the variance of the model parameters to a range that takes into account the uncertainty of using a linear elastic model to calculate displacements in a material that might be better characterized by a more complicated, anisotropic, and/or spatially variable rheology (Sanz et al., 2007; Sanz et al., 2008).

We used the Metropolis–Hastings MCMC method to calculate the posterior probability, $P(m|x)$, of each of the model parameters for which the inversion was performed (Fig. 8). The joint posterior pdf is a nine-dimensional probability distribution, with each of its axes representing the nine model parameters required for the calculation of bedding-plane displacements. Such a distribution is difficult to visualize, and so we present the marginal posterior pdfs by collapsing all dimensions of the joint pdf excepting that of the model parameter of interest onto the dimension of this model parameter (Fig. 8). The resulting pdf shows the variability that characterizes each model parameter, but does not capture the covariation of the different model parameters with one another. For each of the model parameters, we report the value for the best-fitting scenario as italic numbers, the mean of the simulated posterior pdfs as bold numbers, and the 95% range in the simulated model parameter pdfs in parentheses in each of the panels.

The simulations reveal substantial variation in the model parameters such that a variety of their values may produce similarly good fits to the observed elevations (Fig. 8). For many of the model parameters, mean values of the simulation are similar to the best-fitting values, although agreement is substantially less for those distributions that are highly skewed or uncertain (such as ν, $\varepsilon_{xx}/\varepsilon_{xy}$ and $\varepsilon_{xx}/\varepsilon_{yy}$). Nonetheless, the model places broad bounds on fault geometries that may plausibly create the observed displacements. In some cases relatively large values of Poisson's ratio (0.23–0.49) are allowed, which implies that the single-layer models favor a rheology that undergoes minimum volume change during deformation. Considering the range of values produced by the simulation, the fault tip at the center of the fold is expected to be only a few kilometers below the surface at the time of deformation, and is currently

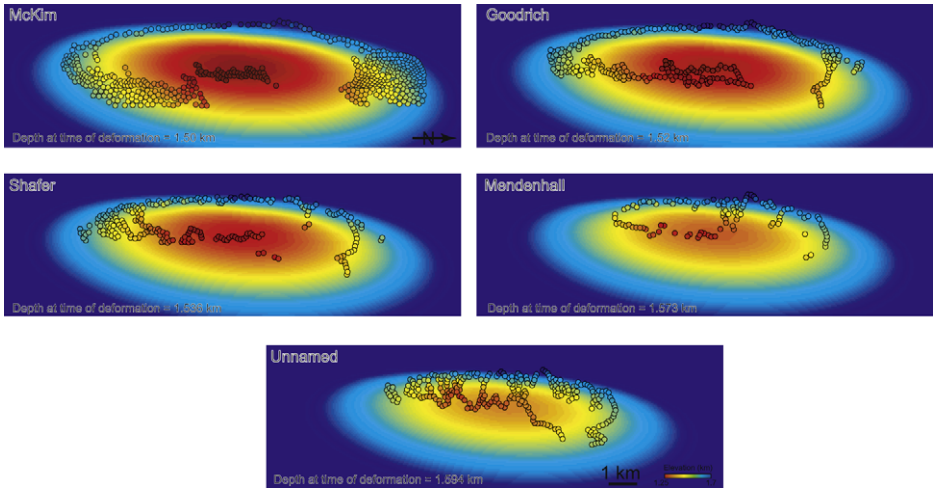

Fig. 9. Observed (filled circles) and predicted (shaded background) elevations of the McKim, Goodrich, Shafer, Mendenhall, and Unnamed surfaces produced by movement along the best-fitting modeled fault geometry that slips in response to the best-fitting remote loading conditions. Color and map-view scale are identical between plots. The inferred depth below the surface of each of these layers at the time of deformation is noted in each of the panels.

predicted to be only several hundred meters below the level of exposure. The down-dip extent of the modeled fault is between 4.5–10.0 km, and the along-strike width of the fault is 13.0–23.5 km.

Next, we performed our inversions using all five of the mapped layers that define the geometry of the Raplee Ridge monocline. The best-fitting multilayer model elevations were similar to those observed (Figs. 9 and 10). The extensive exposure of the McKim, Goodrich, and Shafer surfaces causes the model to most accurately characterize this geometry (Fig. 9). Surfaces lower in the stratigraphy are not fit as well due to the fact that the number of points extracted

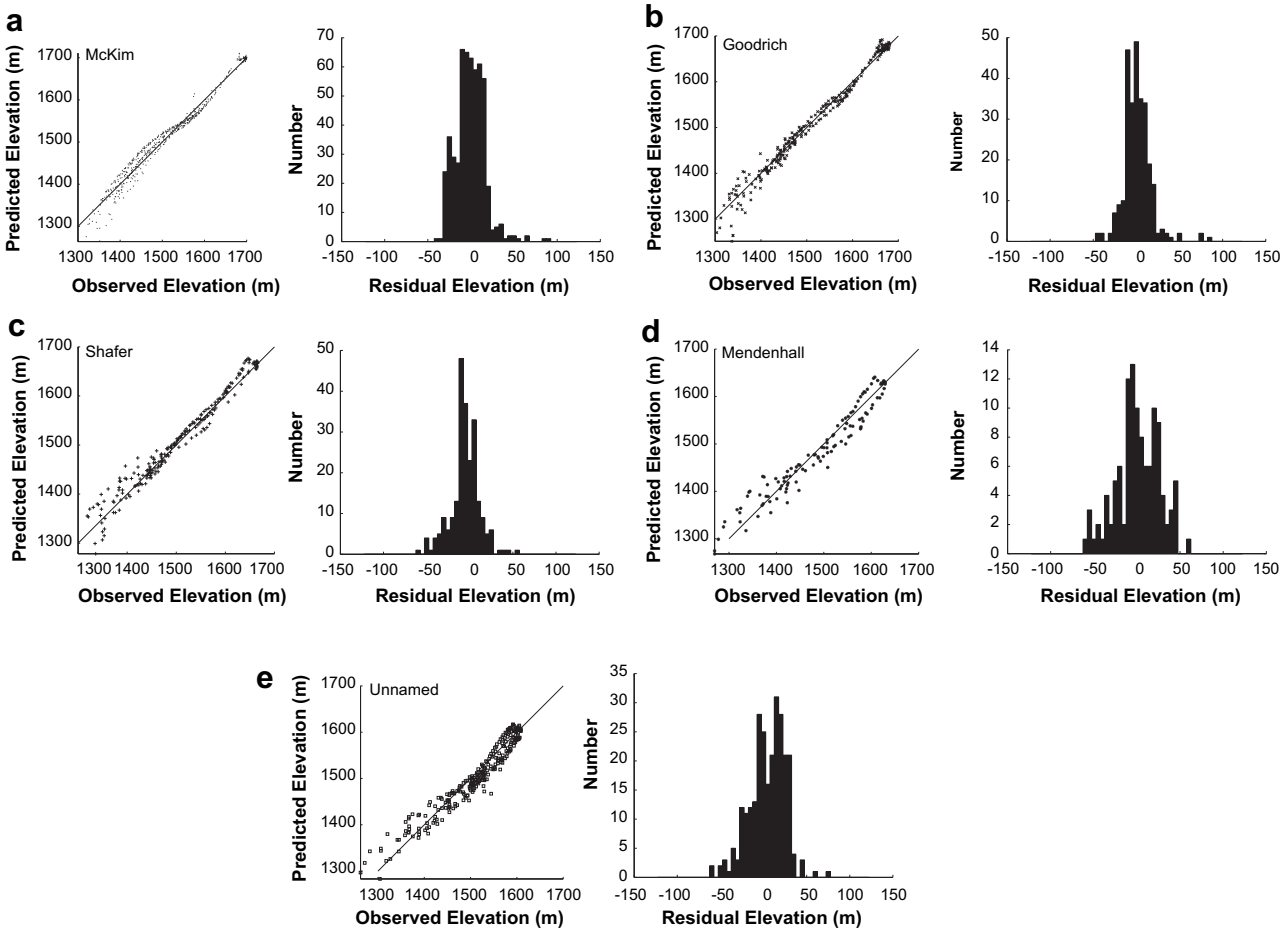

Fig. 10. Observed and modeled elevations (left panels) and histogram of residual elevations (defined in Fig. 6) for best-fitting fault geometry and loading conditions, when considering multiple layers in the model inversion. Observed vs. predicted elevations and residual histograms shown for the (a) McKim, (b) Goodrich, (c) Shafer, (d) Mendenhall, and (e) Unnamed surfaces.

along these surfaces are fewer, and consequently their weight is less in the inversion. This effect is most pronounced for the Mendenhall and Unnamed surfaces, both of which show larger misfit than their counterparts higher in the stratigraphic section (Figs. 9 and 10). When comparing observed versus predicted elevations for the multilayer models (Fig. 10), a slight but systematic underestimation of elevations within the McKim and Goodrich surfaces are observed for elevations of ~1600 m. These points flank the upper-most crest of the fold along the McKim surface, and their misfit arises because the fold is more cylindrical at its crest than might be expected for the simple elliptical fault geometry assumed in this study. Nonetheless, the best-fitting model geometry produces generally unbiased estimates of the elevations across all surfaces (Fig. 10): model residuals for the McKim, Goodrich, Shafer, Mendenhall, and Unnamed surface have means of −1.0, 1.2, −5.3, 1.0, and 4.6 m, respectively, with a mean residual of 7.6×10^{-15} m when considering all points from all layers. The variation within residuals was similar across the McKim, Goodrich, and Shafer surfaces, with standard deviations equaling 16.9, 15.9 and 16.8 m, respectively. However, the fewer points extracted along the less-well-exposed Mendenhall and Unnamed surfaces resulted in higher standard deviations of 25.0 and 20.7 m, respectively.

The best-fitting model parameters deduced when using all of the mapped layers (Figs. 9–11) shared affinity to those derived using only the McKim surface (Figs. 7 and 8). The dimensions of the fold were similar, although the underlying fault was slightly wider in the along-strike direction when using all mapped layers (Fig. 11, italic numbers in each model parameter panel). In addition, the best-fitting model that uses all of the layers favors a deeper fault tip-line at the center of the fold in comparison to the single-layer models. The root-mean-squared error for the best-fitting model was 18.1 m, slightly larger than the single-layer model.

The joint posterior distribution of model parameters estimated using the Metropolis–Hasting sampler permitted sets of fault geometries and loading conditions that were generally consistent with those derived from the single-layer models (Fig. 11). However, inversions that utilized observations from multiple stratigraphic layers generally tended to permit a wider range of model parameters than did single-layer inversions (Figs. 8 and 11). Mean values of the calculated posterior pdfs were similar to those calculated using the best-fitting model. As with the best-fitting modeled fault depth, the range of fault depths allowed by the multilayer inversion tended to be deeper than those predicted using only data from the McKim surface. Unlike single-layer model results, values of

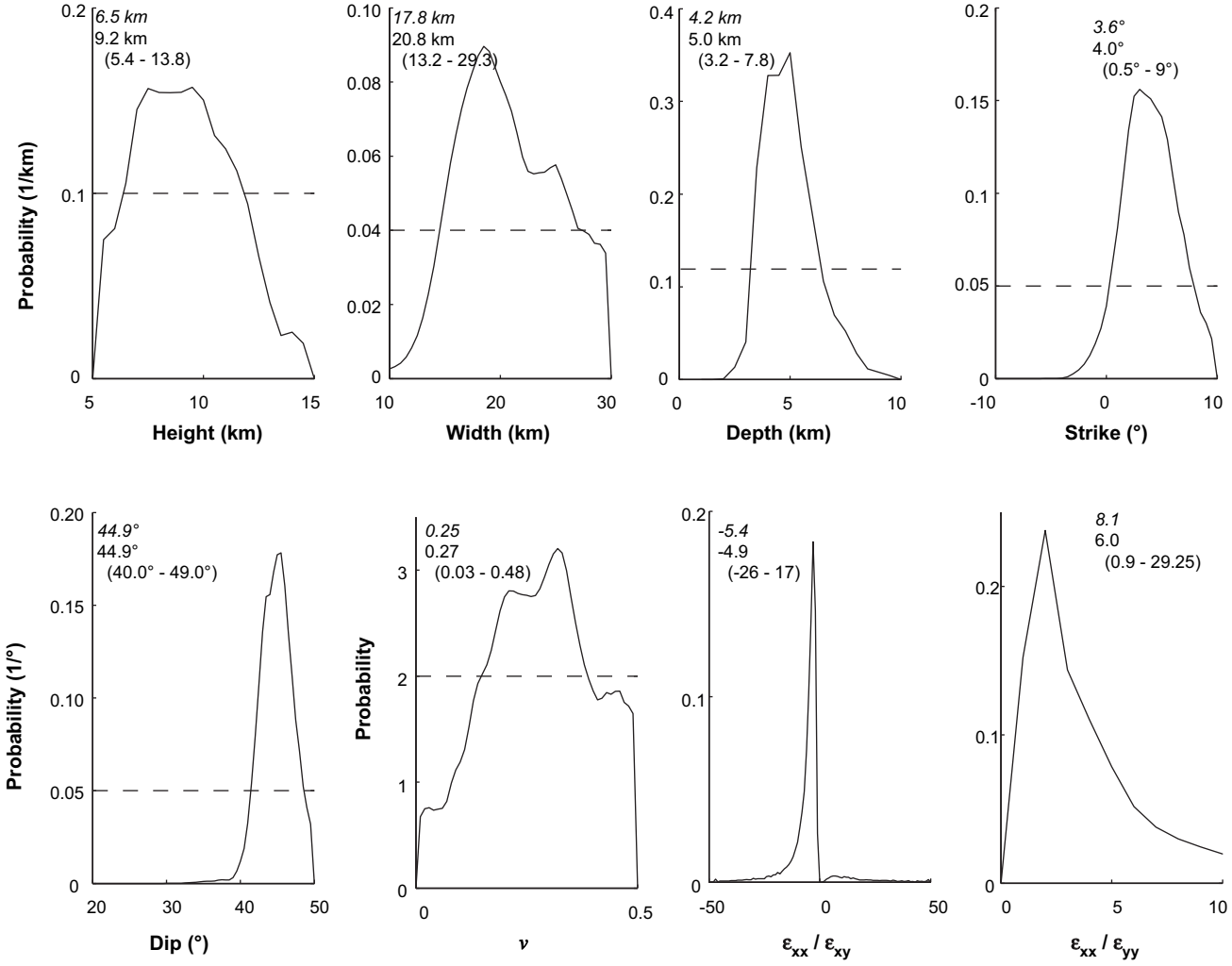

Fig. 11. Posterior probability density functions of each of the model parameters for multiple layer inversions. In each panel, the solid line denotes the probability density of each model parameter given the elevations observed along the McKim surface, while the dashed lines show the prior probability (assumed uniform in this study) assumed for the model parameters. Numbers in italics represent the value of each parameter for the best-fitting model, while solid bold numbers represent the mean value produced by all simulations. The range shown in parentheses represents the 95% bounds on the model parameter values determined from the posterior probability density function.

Poisson's ratio permitted by the multilayer models spanned the range from 0.03–0.48, indicating that this parameter may not be well resolved by such an inversion. Nonetheless, both sets of models predict that the underlying fault dips steeply to the east. In addition, the down-dip extent of the fault is similar to the single-layer model (5.5–13.8 km), while the along-strike width of the fault is inferred to be between 13.2–29.3 km (Fig. 11).

6. Discussion

This study builds on our previous work, in which we used the elevations extracted from the McKim limestone in combination with the BEM to interpolate the geometry of this surface and infer the fault geometry and regional strain. The single-layer models created as part of the current study are similar to those reported in our previous work with two important differences. First, previous work fixed Poisson's ratio to a value of 0.25 when determining the best-fitting and posterior probability densities of the model parameters, while in the current study, we treat this ratio as a free parameter in the inversion. By allowing Poisson's ratio to change, the down-dip height of the fault decreased, while the depth to its upper edge increased. In addition, the larger best-fitting value for Poisson's ratio is associated with a more steeply dipping fault. Second, previous work did not consider the number of degrees of freedom when estimating $P(x|m)$. This had the effect of causing the model parameter posterior distributions to have less variance than those determined in this study. Given the large uncertainties associated with the model itself (discussed below), the higher variance distributions reported in this study likely provide a more realistic estimate of the uncertainties in model parameters than those reported previously.

In addition to expanding the inversion methodology to accommodate observations of bedding rotations and displacements of multiple layers, we explored the impact that spatial resolution and precision of different sources of elevation data might have on the inversions. The standard deviation of the difference between the NED-10 and NED-30 elevations when compared to the ALSM data was found to be ~25% of the RMS error produced by the best-fitting modeled elevations. Thus, given the uncertainties in applying such an idealized model to a complex fold, the NED-10 or NED-30 datasets would have likely been adequate for this analysis. We did find the ALSM data to be invaluable when identifying the extent of the bedding surfaces in the elevation data and the field. In fact, many outcrops that define the fold's geometry are not visible when using the NED-10 or NED-30 datasets (Fig. 3). Thus, while the precise ALSM mapping may not have increased the precision of elevation measurements used as input for inversions, it aided in the identification of those areas from which such elevation measurements were extracted.

The methods presented here provide a new, mechanically based way of interpolating the geometry of three-dimensional fault-related folds and imaging the geometry of the underlying faults. As such, the results must be viewed in the context of the simplifying assumptions of the mechanical models upon which the approach is based. In particular, the BEM idealizes the crust as a homogeneous linear elastic half-space into which elements that may accommodate slip and opening are embedded. In reality, the rocks currently exposed within the Raplee monocline likely deformed anisotropically, elastically or visco-elastically. In addition, the study infers the geometry of a fault that has not been imaged in the subsurface. Importantly, some of the geometric parameters of the fault are poorly defined, especially the down-dip extent of the fault (fault height), which results from the narrow cross-strike aperture of the topographic swath. Thus, our inversion results indicate that the deep geometry of the structure is poorly imaged, and as such, geometries that serve as a deep backthrust to the Comb Ridge fault, or a ramp-flat geometry that transfers horizontal slip into the fold along a decollement at some depth are certainly possible. The geometry of the fault was chosen for simplicity: alternative deeper geometries would likely be permitted by our model, but their geometric properties would be similarly poorly defined as the bottom edge of the elliptical fault used in this study. Given that each of these more complicated geometries would require far more, and far more poorly defined, free parameters, we view the results from the elliptical fault geometry as realistic to first-order, but acknowledge that there is little that can be said with confidence about the deeper aspects of the fault's geometry based on the limited surface observations available.

In spite of these simplifying assumptions, the method predicts fold shapes consistent with elevations of specific bedding surfaces observed using the ALSM data. In addition, the original work of Kelley (1955) on monoclines of the Colorado Plateau posits the existence of a slight component of left-lateral shear across the Comb Ridge structure. This sense-of-shear is consistent with the slight sinistral shear produced by the inverted fault strike and remote strain conditions. Nonetheless, to validate such an approach, similar analyses should be performed in areas where subsurface imaging allows comparison of these imaged geometries with those modeled using surface data.

The success of the BEM in accurately depicting the geometry of Raplee Ridge monocline indicates either that the approximation of linear elasticity serves as an adequate characterization of the rheology of the folded materials, or that different rheological properties may produce similar observed fold geometries by allowing the underlying geometry of the slipping fault to change as well. While the Metropolis-Hastings sampler provides estimates of the uncertainties within model parameters that arise from the characterization of the uncertainties in the data, the uncertainties associated with the inappropriateness of the simplified rheology in our model is not captured. In the future, numerical experiments using finite element models that can consider more complicated rheologies may be used to assess the trade-offs between the loading conditions (represented by the far-field strain conditions and the underlying fault geometry), rheology, and observed surface displacements. The results from a suite of experiments employing different rheologies and analyzed using the methods presented in this work may be compared with one another to assess the degree of uncertainty that is associated with the choice of the rheology of the folded material. This choice may impact the parameters such as fault geometry that are inferred by this approach, and so by having independent estimates of these values, it might be possible to discern the most appropriate rheological model for these types of folds.

7. Conclusions

We present a method that uses the elevations of stratigraphic marker layers exposed within fault-related folds to infer the underlying fault geometry, loading conditions, and Poisson's ratio of the folded material, assuming that deformation is due to the release of stress along a frictionless elliptical fault embedded in a homogeneous linear elastic half-space. This method may be applied to situations in which a single bedding surface is exposed, or multiple surfaces have been deformed and exhumed. In addition to bedding-plane elevations, the orientation of units at various locations in a particular part of the stratigraphic section may be used to further constrain the geometry of the fold and underlying fault. Using a Bayesian Markov–Chain Monte Carlo method, we determined the fault geometry, loading conditions, and elastic parameters that best explain the observed surface displacements, as well as the variation within and covariation between these

model parameters. This allowed us to understand the degree to which the data constrain model parameters and the various combinations of model parameters that may produce the observed surface displacements.

We applied these methods to the Raplee Ridge monocline, located in southeastern Utah, where ALSM data define the geometry of exposed bedding surfaces. While we found that the resolution and precision of the ALSM data are unnecessary for inferring the fault geometry and loading conditions using our approach, these data were necessary for the mapping of the spatial distribution of surface outcrops. Both single-layer and multilayer inversions agree remarkably well with observations, and image a fault that is broadly constrained to be ~4.5–14 km in down-dip height, 13–30 km in along-strike width, with a tip-line 2.0–9.5 km below the surface at the time of deformation. Poisson's ratio was not well resolved by the inversion. The consistency of the simplified (and likely unrealistic) rheology of the folded material with the observed geometry might suggest that surface displacements may reveal little about the rheology of the folded rock when viewed in isolation from factors such as fault geometry and loading conditions.

Acknowledgements

DDP and IM acknowledge support from the National Science Foundation's Collaborations in Mathematical Geosciences grant no. CMG-0417521.

References

Allmendinger, R.W., 1998. Inverse and forward numerical modeling of trishear fault-propagation folds. Tectonics 17, 640–656.
Allmendinger, R.W., Shaw, J., 2000. Estimation of fault propagation distance from fold shape; implications for earthquake hazard assessment. Geology 28 (12), 1099–1102.
Bayes, T., 1763. An essay towards solving a problem in the doctrine of chances. R. Soc. Lond. Philos. Trans. 53, 370–418.
Bellahsen, N., Fiore, P.E., Pollard, D.D., 2006. From spatial variation of fracture patterns to fold kinematics: a geomechanical approach. Geophys. Res. Lett. 33, L02301.
Bump, A.P., 2003. Reactivation, trishear modeling, and folded basement in Laramide uplifts. GSA Today March, 4–10.
Bump, A.P., Ahlgren, S., Davis, G.H., 1997. The Waterpocket Fold, a tale of two uplifts, Capitol Reef National Park, Utah. EOS Trans. Am. Geophys. Union 78 (46), 701.
Bürgmann, R., Kogan, M.G., Steblov, G.M., Hilley, G.E., Levin, V.E., Apel, E., 2005. Interseismic coupling and asperity distribution along the Kamchatka subduction zone. J. Geophys. Res., B, Solid Earth Planets 110, B07405.1–B7405.17.
Cardozo, N., 2008. Trishear in 3D. Algorithms, implementation, and limitations. J. Struct. Geol. 30 (3), 327–340.
Casey, M., Butler, R.W.H., 2004. Modelling approaches to understanding fold development: implications for hydrocarbon reservoirs. Mar. Pet. Geol. 21, 933–946.
Cooke, M.L., Pollard, D.D., 1997. Bedding-plane slip in initial stages of fault related folding. J. Struct. Geol. 19, 567–581.
Davis, G.H., 1978. The monocline fold pattern of the Colorado Plateau. In: Matthews, V. (Ed.), Laramide Folding Associated with Basement Block Faulting in the Western US Geological Society of America Memoirs 151, pp. 215–233.
Davis, G.H., 1979. Laramide folding and faulting in southern. Arizona. Am. J. Sci. 279, 543–569.
Davis, G.H., 1999. Structural geology of the Colorado Plateau Region of Southern Utah, with special emphasis on deformation bands. Geological Society of America Special Paper 342.
Erslev, E.A., 1991. Trishear fault-propagation folding. Geology 19, 617–620.
Fiore, P.E., Pollard, D.D., Currin, W.R., Miner, D.M., 2007. Mechanical and stratigraphic constraints on the evolution of faulting at Elk Hills, California. AAPG Bulletin 91 (3), 321–341.
Gratier, J.P., Guillier, B., Delorme, A., Odone, F., 1991. Restoration and balanced cross section of a folded and faulted surface by computer program: principle and application. J. Struct. Geol. 13, 111–115.
Gregory, H.E., Moore, R.C., 1931. The Kaiparowits Regions, a geographic and geologic reconnaissance of parts of Utah and Arizona. US Geological Survey Professional Paper 164.
Guiton, M.L.E., Leroy, Y.M., Sassi, W., 2003. Activation of diffuse discontinuities and folding of sedimentary layers. J. Geophys. Res. 108 (B4), 2183.
Hilley, G.E., Young, J.J., 2008a. Deducing paleoearthquake timing and recurrence from paleoseismic data, Part I: Evaluation of new Bayesian Markov-Chain Monte Carlo simulation methods applied to excavations with continuous peat growth. Bull. Seismol. Soc. Am. 98, 383–406.
Hilley, G.E., Young, J.J., 2008b. Deducing paleoearthquake timing and recurrence from paleoseismic data, Part II: Analysis of paleoseismic excavation data and earthquake behavior along the central and southern San Andreas fault. Bull. Seismol. Soc. Am. 98, 407–439.
Hodgson, R.A., 1961. Regional study of jointing in Comb Ridge-Navajo Mountain area, Arizona and Utah. AAPG Bull. 45, 1–38.
Huntoon, P.W., 1993. Influence of inherited Precambrian basement structure on the localization and form of Laramide monoclines, Grand Canyon, Arizona. In: Schmidt, C.J., Chase, R.B., Erslev, E.A. (Eds.), Laramide Basement Deformation in the Rocky Mountain Foreland of the Western United States. Geological Society of America Special Paper No. 280, pp. 243–256.
Huntoon, P.W., Sears, J.W., 1975. Bright Angel and Eminence faults, eastern Grand Canyon, Arizona. Geol. Soc. Am. Bull. 86, 465–472.
Isaaks, E.H., 1989. Applied Geostatistics. Oxford University Press, New York.
Jaeger, J.C., Cook, N.G.W., 1969. Fundamentals of Rock Mechanics. Methuen and Co Ltd, London.
Jamison, W.R., 1987. Geometric analysis of fold development in overthrust terranes. J. Struct. Geol. 9, 207–219.
Jentgen, R.W., 1977. Pennsylvanian Rocks in the San Juan Basin, New Mexico and Colorado, in: New Mexico Geological Society, 28th Field Conference Guidebook - Guidebook of San Juan Basin III, Northwestern New Mexico, Farmington, N.W. United States, No. 28. New Mexico Geological Society, pp. 129–132.
Johnson, K.M., Johnson, A.M., 2001. Mechanical analysis of the geometry of forced-folds. J. Struct. Geol. 24, 401–410.
Johnson, K.M., Johnson, A.M., 2002. Mechanical models of trishear-like folds. J. Struct. Geol. 24, 277–287.
Kelley, V.C., 1955. Monoclines of the. Colorado Plateau. Bull. Geol. Soc. Am. 66, 789–804.
Maerten, F., Maerten, L., 2008. Iterative 3D BEM solver on complex fault geometry using angular dislocation approach in heterogeneous, isotropic elastic whole or half-space. Boundary Elements and Other Mesh Reduction 30. doi:10.2495/BE080201.
Maerten, F., Resor, P., Pollard, D.D., Maerten, L., 2005. Inverting for slip on three-dimensional fault surfaces using angular dislocations. Bull. Seismol. Soc. Am. 95, 1654–1665.
Maerten, L., Gillespie, P., Daniel, J.-M., 2006. 3-D geomechanical modeling for constraint of subseismic fault simulation. AAPG Bull. 90, 1337–1358.
Metropolis, N., Rosenbluth, A.W., Rosenbluth, M.N., Teller, A.H., Teller, E., 1953. Equations of state calculations by fast computing machines. J. Chem. Phys. 21, 1087–1091.
Mitra, S., 1990. Fault-propagation folds: geometry, kinematic evolution, and hydrocarbon traps. AAPG Bull. 74, 921–945.
Mynatt, I., Seyum, S., Pollard, D.D., 2009. Fracture initiation, development and reactivation in folded sedimentary rocks at Raplee Ridge, UT. J. Struct. Geol. 31 (10), 1100–1113.
Mynatt, I., Hilley, G.E., Pollard, D.D., 2007. Inferring fault characteristics using fold geometry constrained by Airborne Laser Swath Mapping at Raplee Ridge, Utah. Geophys. Res. Lett. 34, L16315.
Narr, W., Suppe, J., 1994. Kinematics of basement-involved compressive structures. Am. J. Sci. 294, 802–860.
O'Sullivan, R.B., 1965. Geology of the Cedar Mesa-Boundary Butte Area, San Juan County, Utah, in: US Geological Survey Bulletin, Report B 1186. USGS, Publications of the US Geological Survey, Reston, VA, 128 pp.
Pollitz, F.F., 2003. Transient rheology of the uppermost mantle beneath the Mojave Desert, California. Earth Planet. Sci. Lett. 215, 89–104.
Reches, Z., 1978. Development of monoclines, Part I: Structure of the Palisades Creek branch of the east Kaibab monocline, Grand Canyon, Arizona. In: Matthews, V. (Ed.), Laramide Folding Associated with Basement Block Faulting in Western United States. Geological Society of America Memoirs 151, pp. 235–271.
Reches, Z., Johnson, A.M., 1978. Development of monoclines, Part II: Theoretical analysis of monoclines. In: Matthews, V. (Ed.), Laramide Folding Associated with Basement Block Faulting in Western United States. Geological Society of America Memoirs 151, pp. 273–311.
Sanz, P.F., Borja, R.I., Pollard, D.D., 2007. Mechanical aspects of thrust faulting driven by far-field compression and their implications for fold geometry. Acta Geotech 2, 17–31.
Sanz, P.F., Pollard, D.D., Allwardt, P.F., Borja, R.I., 2008. Mechanical models of fracture reactivation and slip on bedding surfaces during folding of the asymmetric anticline at Sheep Mountain. Wyoming. J. Struct. Geol. 30, 1177–1191.
Shamir, G., Eyal, Y., 1995. Elastic modeling of fault-driven monoclinal fold patterns. Tectonophysics 245, 13–24.
Suppe, J., 1985. Principles of Structural Geology. Prentice Hall, Inc., Englewood Cliffs, NJ.
Tamagawa, T., Pollard, D.D., 2008. Fracture permeability created by perturbed stress fields around active faults in a fractured basement reservoir. AAPG Bull. 92, 743–764.
Thomas, A.L., 1993. Poly3D: a three-dimensional, polygonal element, displacement discontinuity boundary element computer program with applications to fractures, faults, and cavities in the Earth's crust. Stanford University.
Tindall, S.E., Davis, G.H., 1999. Monocline development by oblique-slip fault-propagation folding; the East Kaibab Monocline, Colorado Plateau. Utah. J. Struct. Geol. 21 (10), 1303–1320.
Willemse, E.J.M., Pollard, D.D., Aydin, A., 1996. Three-dimensional analyses of slip distributions on normal fault arrays with consequences for fault scaling. J. Struct. Geol. 18 (2-3), 295–309.
Wolkowinsky, A.J., Granger, D.E., 2004. Early Pleistocene incision of the San Juan River, Utah, dated with ^{26}Al and ^{10}Be. Geology 32, 749–752.
Ziony, J.I., 1966. Analysis of Systematic Jointing in Part of the Monument Upwarp, Southeastern Utah. University of California, Los Angeles, CA.